

## A SUBARU PENCIL-BEAM SEARCH FOR $M_R \sim 27$ TRANS-NEPTUNIAN BODIES<sup>1</sup>

CESAR I. FUENTES<sup>2</sup>, MATTHEW R. GEORGE<sup>2,3</sup>, MATTHEW J. HOLMAN<sup>2</sup>

SUBMITTED TO APJL: September 22, 2008

### ABSTRACT

We present the results of an archival search for Trans-neptunian objects (TNOs) in an ecliptic field observed with Subaru in 2002. The depth of the search allowed us to find 20 new TNOs with magnitudes between  $R = 24$  and 27. We fit a double power law model to the data; the most likely values for the bright and faint power law exponents are  $\alpha_1 = 0.73_{-0.09}^{+0.08}$  and  $\alpha_2 = 0.20_{-0.14}^{+0.12}$ ; the differential number density at  $R = 23$  is  $\sigma_{23} = 1.46_{-0.12}^{+0.14}$  and the break magnitude is  $R_{eq} = 25.0_{-0.6}^{+0.8}$ . This is the most precise measurement of the break in the TNO luminosity function to date. The break in the size distribution corresponds to a diameter of  $D = 90 \pm 30$  km assuming a 4% albedo.

*Subject headings:* Kuiper Belt – Solar System: formation

### 1. INTRODUCTION

The TNO size distribution is the result of the formation and collisional history of its members. Models of the physical evolution assume the processes at play result in a characteristic power law size distribution. In the model of Pan & Sari (2005) of strengthless TNOs, the collisional evolution of the objects leads to an evolving size distribution that changes slope at the size at which the collisional lifetime of an object equals the age of the system. This analytical result confirms those obtained from numerical simulations (Kenyon & Luu 1999; Davis et al. 1999; Kenyon & Bromley 2004). The precise location of the break in the size distribution is an important measurement to link TNO formation and evolution models to the current TNO population (see Kenyon et al. 2008 for a review).

The TNO luminosity function is defined by the distance, albedo, and size distributions of TNOs, and it is readily observed. The distance distribution exhibits a sharp edge at 50 AU (Trujillo et al. 2001) that has been observed in other surveys (Gladman et al. 2001; Fuentes & Holman 2008). Though it is customary to use a 4% albedo, correlations with size have been reported (see Stansberry et al. 2008 for a review). After making sensible assumptions for the albedo and distances of the observed TNOs, the size distribution can be derived from the luminosity function. Several searches have been completed (see Bernstein et al. 2004; Fuentes & Holman 2008 for a review), the deepest being the search by Bernstein et al. (2004) with the *Hubble Space Telescope* (HST). While previous results sampled the size distribution up to magnitude  $R = 26$  and were consistent with a power law luminosity function, the Bernstein et al. (2004) survey found a significant underabundance of objects at  $R \sim 28$ , compared to that predicted from extrapolating the luminosity function at brighter magnitudes. They concluded a break in the luminosity function must occur between  $R \sim 25$  and 28.

Since Bernstein et al. (2004) announced their results, a number of ground-based surveys for fainter TNOs have been conducted in an effort to bridge the divide between the brighter ( $R \sim 23$ ) TNOs found through wide-field searches such as the Deep Ecliptic Survey (Elliot et al. 2005) and the Canada-France Ecliptic Plane Survey (Jones et al. 2006) and those found by Bernstein et al. (2004). Fuentes & Holman (2008) discovered 82 TNOs in an archival search of Subaru data. This survey reached a limiting magnitude of  $R = 25.7$  and successfully detected the break in the luminosity function. In the present work we build upon that earlier work, increasing the limiting magnitude of ground-based surveys to  $R \sim 27$  and further narrowing the gap between ground-based and space-based TNO surveys. Constraints on even fainter objects have been placed by stellar occultation surveys (Bickerton et al. 2008; Zhang et al. 2008).

We present the details of the data in the next section. § 3 outlines the method used to analyze and search for TNOs in the data. The characterization of the search using a synthetic population is presented in § 4. In § 5 and § 6 we present our results and discuss what they imply for the formation and evolution of the TNO population.

### 2. DATA

The apparent motion of solar system bodies limits the useful exposure time to the period required for an object to move a PSF width; longer exposures spread the signal along a trail and, correspondingly, increase the contribution of the sky background. To overcome this, we consider a series of short exposures and shift the successive images to compensate for the motion of the object. In this way the signal from the source can dominate the noise from the background. This “pencil beam” or “digital tracking” approach has been successfully applied in searches for TNOs and outer planet satellites (Allen et al. 2001; Gladman et al. 2001; Holman et al. 2004; Kavelaars et al. 2004; Fraser et al. 2008).

Using Subaru’s electronic archive SMOKA (Ichikawa 2002), we identified a data set well suited to such a search, a series of 148 consecutive 120 s exposures of a single, ecliptic field observed with Subaru on UT 2002 September 2 over the course of 8 hours. These data were

<sup>1</sup> Based on data collected at Subaru Telescope, which is operated by the National Astronomical Observatory of Japan.

<sup>2</sup> Harvard-Smithsonian Center for Astrophysics, 60 Garden Street, Cambridge, MA 02138, USA; cfuentes@cfa.harvard.edu

<sup>3</sup> Current Address: Department of Astronomy, University of California at Berkeley, Berkeley, CA 94720, USA

collected with Suprime-Cam (Miyazaki et al. 2002), a 10-CCD mosaic camera with a  $34' \times 27'$  field of view and an image scale of  $0''.202 \text{ pix}^{-1}$ . It is our understanding that these data were originally collected for the Subaru Main Belt Asteroid Survey (see Yoshida & Nakamura 2007). The field, R.A. 22:41:38, Dec -07:37:35, is less than  $1^\circ$  from the ecliptic and was observed near opposition using the “Cousins R” filter. Although brief intervals of clouds are apparent from the images, the night was mostly photometric, with stable seeing of  $\sim 0''.7$ .

We trimmed, bias subtracted and flat divided the images with calibrations obtained on the same night and the next one using standard IRAF<sup>4</sup> routines.

### 3. MOVING OBJECT DETECTION

We determined an astrometric solution for each individual CCD using the 2MASS point source catalog (Cutri et al. 2003). The RMS of the solution was  $\sim 0''.2$ , comparable to that of the catalog and much smaller than the typical seeing. We then registered every image to the same astrometric reference.

Next, we inserted a population of synthetic objects that will be later used to determine the efficiency of our search (the details of this process are given in § 4).

To detect TNOs moving at any physically plausible velocity, we defined a grid of rates, parallel and perpendicular to the ecliptic. A TNO at a typical distance of 42 AU exhibits a parallactic motion of  $\sim 3'' \text{ h}^{-1}$ , moving about 120 pixels over the length of the observations. We searched rates from  $0''.7$  to  $5''.1 \text{ h}^{-1}$  for the parallel rate to cover the range between  $\sim 20$  and 200 AU, and perpendicular rates in the range  $-1''.4$  to  $1''.4 \text{ h}^{-1}$ . Furthermore, we restricted our attention to directions of apparent motion within  $15^\circ$  of the ecliptic, which nevertheless permits the detection of highly inclined TNOs. We searched these rates with a resolution of  $0''.1 \text{ h}^{-1}$  along both axes (this resolution ensures that the signal in the first image can be aligned with that in the last for any object).

Prior to combining the images, we used the ISIS package (Alard 2000) to PSF match and subtract a template from each individual exposure, thus eliminating any source that is stationary and of constant brightness. For each individual CCD, the template image was the median combination of 10 of the best-seeing images. Saturated stars were masked at this point to avoid spurious detections due to imperfect subtraction.

To optimally combine the 148 images we defined a “weight” for each image based on both its sky background and seeing:  $w_i = \sigma_i^{-2} \theta_i^{-2} (\sum_j \sigma_j^{-2} \theta_j^{-2})^{-1}$ , where  $\theta$  is the FWHM and  $\sigma$  is the standard deviation of the background in counts. We defined a reference time to be the weighted average of the exposure mid-times. For each of the 736 combinations of parallel and perpendicular rates we shifted all subtracted images to the reference time and computed the weighted average of them.

We searched each of the “shifted and added” images for point sources that corresponded to real or implanted objects moving at the corresponding rate. For

this we used a combination of the SExtractor package (Bertin & Arnouts 1996) and a wavelet source detection routine (Petit et al. 2004), each with a  $3\sigma$  detection threshold. These two approaches rely on very different image properties and, thus, have different noise characteristics. We have found that the intersection of the results from these two routines strongly discriminates against false detections. Nevertheless, we find  $\sim 300$  detections per coadded CCD at each combination of rates parallel and perpendicular to the ecliptic.

We comb through these with an automated search algorithm. The algorithm considers all detections in all of the parallel and perpendicular rate combinations (roughly  $2.2 \times 10^5$  detections per CCD), projects them on the sky plane, and then searches for clusters of detections. Assuming each cluster corresponds to a moving object detected in one or more of the coadded images for rates close to the real, or synthetic, one, the code selects the single detection from every cluster that has the smallest ellipticity and largest flux. We visually inspect the resulting  $\sim 300$  candidates per CCD in order to reject any obvious spurious detections; those rejected are typically poorly subtracted stars that were not adequately masked, or cosmic rays that resulted in multiple detections. This inspection process is extremely fast and decreases the number of possible moving objects to  $\sim 60$  per CCD. We further examine each of these remaining candidates to determine the parallel and perpendicular rates that yield the PSF that best resembles a normal one. In this way we visually found the best rate of motion. In this process another 40% of the remaining objects were rejected.

The novelty in this method is the initial automated search and visual filter for candidates that are later checked by blinking through different rates. The alternatives are a fully automated search algorithm run at a higher detection threshold to eliminate false positives (Bernstein et al. 2004) or a visual search through the whole field and all possible rates (Gladman et al. 2001). We expect that a fully visual search would be more sensitive, leaving aside the issue of human fatigue. To test this we completed a visual search of 20% of the area (two of the ten CCDs). In this test we visually confirmed or rejected potential candidates identified by the two source detection algorithms, as was done by Holman et al. (2004). The comparison showed our approach to be  $\sim 10\%$  less sensitive compared to a visual search, roughly independent of magnitude and rate.

### 4. CONTROL POPULATION AND DETECTION EFFICIENCY

To calibrate our search we used a control population of objects that resemble real TNOs both astrometrically and photometrically. We considered a range of distances (30 – 200 AU) and magnitudes ( $R = 24.5 - 29.5$ ), as well as the full range of eccentricities and inclinations to create a population of synthetic TNOs. Ephemerides for this population were created using a modified version of the *Orbit* routines (Bernstein & Khushalani 2000).

For each CCD  $\sim 10$  bright stars were used to determine a PSF model. These stars are also used to account for changes in the seeing and the atmospheric transparency when implanting objects.

We recovered 312 synthetic TNOs and used them to

<sup>4</sup> IRAF is distributed by the National Optical Astronomy Observatories, which are operated by the Association of Universities for Research in Astronomy, Inc., under cooperative agreement with the National Science Foundation.

determine the efficiency as a function of  $R$  magnitude. The result is shown in Figure 1. The detection efficiency is well represented by the following function:

$$\eta(R) = \frac{A}{2} \left( 1 - \tanh \frac{R - R_{50}}{w} \right) \quad (1)$$

where the best fit values are  $A=0.86 \pm 0.07$ ,  $R_{50}=26.76 \pm 0.06$  and  $w=0.38 \pm 0.04$ . The maximum efficiency of our search is 86%, and it reaches half this value at magnitude  $R = 26.76$ .

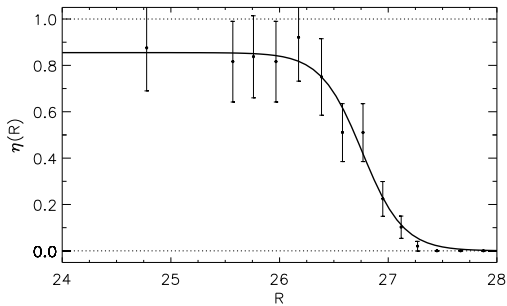


FIG. 1.— Detection efficiency as a function of magnitude. The solid line corresponds to Eq. 1, with best fit values:  $A=0.86 \pm 0.07$ ,  $R_{50}=26.76 \pm 0.06$  and  $w=0.38 \pm 0.04$ .

The USNO-B Catalog was used to tie the photometry of our objects to a standard system. A number of USNO-B stars are unsaturated in our field ( $m_R > 18$ ). The photometric uncertainty of the catalog is 0.3 mag (Monet et al. 2003). Seven isolated stars were selected, and compared to the photometry of an exposure from a photometric portion of the night. The flux  $f_5$  for a 5-pixel ( $1''.01$ ) aperture over a time  $t$  in seconds was found to be:

$$R = 27.45 - 2.5 \log f_5/t. \quad (2)$$

An aperture correction of 0.076 mag is included in this formula.

## 5. RESULTS AND ANALYSIS

Our search resulted in 20 new objects, summarized in Table 1. The distances to these objects are estimated using their parallactic motion, assuming circular orbits. To estimate the uncertainty in these distance estimates, we compare the precision of the parallactic rate to that in Fuentes & Holman (2008) and adopt the uncertainty in those distances (2.5 AU). There are three objects with distances closer than 30 AU; given the poor orbital information we assume these objects are Plutinos and retain them in our sample.

We were able to measure the error in our photometry via comparison of the implanted and recovered magnitudes, plotted in Figure 2. This allowed us to set the aperture correction and include any uncertainty introduced by our method. The net uncertainty is  $\sim 0.2$  mag, similar to the expected variance given the sky background; we adopted it as the  $1-\sigma$  uncertainty for all our detections. As for the accuracy in the rate of motion parallel and perpendicular to the ecliptic is  $\sim 0''.1 \text{ h}^{-1}$ . The corresponding uncertainty in the angle to the ecliptic is  $\sim 3$  deg.

TABLE 1  
TNO PROPERTIES<sup>a</sup>

	$R_{mag}$	R.A.	Decl.	$dR.A./dt$ ( $'' \text{ h}^{-1}$ )	$dDecl./dt$ ( $'' \text{ h}^{-1}$ )	$d_{par}$ (AU)
sd1	26.7	22:40:46.967	-07:28:56.80	-3.19	-1.53	35.5
sd2	24.0	22:40:38.889	-07:34:33.23	-2.99	-1.23	39.2
sd3	24.6	22:40:48.201	-07:33:30.04	-2.99	-1.23	39.2
sd4	26.7	22:42:46.043	-07:25:05.09	-4.39	-1.27	26.8
sd5	26.6	22:42:29.147	-07:34:07.96	-2.80	-1.15	42.1
sd6	25.9	22:42:39.499	-07:34:09.84	-3.55	-1.46	32.4
sd7	25.4	22:42:26.506	-07:34:58.77	-2.67	-1.21	43.6
sd8	25.1	22:42:31.162	-07:36:21.54	-2.71	-1.12	43.6
sd9	25.2	22:42:36.655	-07:28:27.49	-2.28	-0.83	53.6
sd10	25.9	22:42:17.085	-07:24:26.88	-3.19	-1.53	35.5
sd11	24.6	22:42:18.460	-07:35:09.91	-2.89	-1.19	40.6
sd12	26.1	22:41:33.852	-07:39:08.51	-2.99	-1.23	39.2
sd13	26.6	22:41:33.660	-07:40:31.79	-4.03	-1.88	27.5
sd14	26.8	22:40:57.890	-07:44:53.89	-2.89	-1.19	40.6
sd15	26.6	22:41:22.837	-07:42:07.71	-4.22	-1.41	27.5
sd16	25.7	22:41:01.823	-07:35:49.27	-2.86	-1.29	40.6
sd17	26.6	22:41:09.107	-07:25:13.78	-2.78	-0.93	43.6
sd18	24.9	22:41:09.797	-07:26:31.27	-2.71	-1.12	43.6
sd19	26.7	22:41:44.583	-07:31:58.21	-4.71	-1.29	24.9
sd20	26.8	22:42:38.548	-07:47:45.67	-2.44	-1.23	47.2

<sup>a</sup> Positions and rates valid for MJD 52519.451992. The uncertainties can be found in the text.

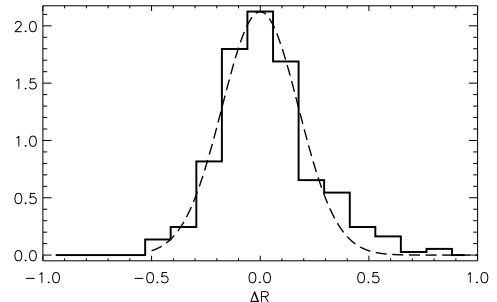


FIG. 2.— Histogram of the magnitude difference between implanted and measured magnitudes  $\Delta R$ . The dashed line is a Gaussian of width 0.18 mag.

With the standard photometry and efficiency function we construct a luminosity function for the 20 objects in this field. The result for this survey is shown on the left panel of Figure 3. The best model for the TNO-number cumulative function is given by the harmonic mean of two power laws, or double power law (DPL), as introduced by Bernstein et al. (2004) and corroborated by Fuentes & Holman (2008). The surface number density for the DPL is given by:

$$\sigma(R) = C \left[ 10^{-\alpha_1(R-23)} + 10^{(\alpha_2-\alpha_1)(R_{eq}-23)-\alpha_2(R-23)} \right]^{-1},$$

$$C = \Sigma_{23} (1 + 10^{(\alpha_2-\alpha_1)(R_{eq}-23)}), \quad (3)$$

where  $\alpha_1$  and  $\alpha_2$  are the exponents for the bright and faint power law behavior of the model;  $\Sigma_{23}$  is the number of objects expected brighter than  $R = 23$  and  $R_{eq}$  corresponds to the magnitude at which both power law behaviors meet. Figure 3 shows the cumulative surface density  $\Sigma(R) = \int_{-\infty}^R \sigma(x) dx$ .

There are not enough objects in this survey alone to constrain the model; however the data follow the previous best estimate for the model (Fuentes & Holman

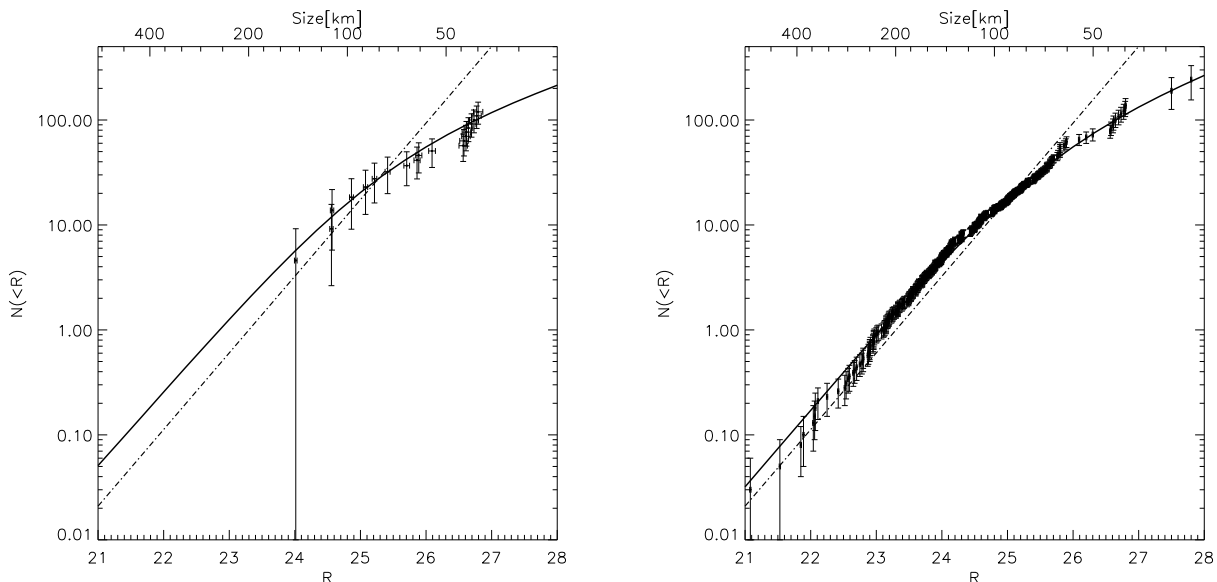


FIG. 3.— The cumulative number density for the objects in our survey is shown on the left panel. The solid line is the best previous model (Fuentes & Holman 2008). All surveys listed in Fuentes & Holman (2008, Table 2) plus those included in this work are shown in the right panel. The most likely model is shown as a solid line (see Fig. 4). The function  $10^{0.73(R-23.3)}$  is the dot-dashed line. The top axis assumes a 4% albedo and every object at 42 AU. The apparent steep slope at  $R \sim 26.7$  is a result of small number statistics and plotting the cumulative, rather than differential, luminosity function.

2008). The previous best parameters were  $\alpha_1=0.7^{+0.2}_{-0.1}$ ,  $\alpha_2=0.3^{+0.2}_{-0.2}$ ,  $\sigma_{23}=2.0^{+0.5}_{-0.5}$  and  $R_{eq}=24.3^{+0.8}_{-0.1}$ , overplotted in Figure 3. Furthermore, this model predicts 21 detections for this search, consistent with the 20 that were found.

We combined our survey with those listed in Fuentes & Holman (2008, Table 2). We only considered objects found at magnitudes at which the search was over 15% of the maximum efficiency. All the objects in our search fulfill this requirement. The total luminosity function is shown in the right panel of Figure 3. The DPL best fit is determined through a Markov Chain Monte Carlo simulation (details in Fuentes & Holman 2008) with  $10^6$  steps, and an acceptance rate of 25%. The posterior distribution function (PDF) for each parameter is plotted in Figure 4; the most likely parameters are given by:  $\alpha_1=0.73^{+0.08}_{-0.09}$ ,  $\alpha_2=0.20^{+0.12}_{-0.14}$ ,  $\sigma_{23}=1.46^{+0.14}_{-0.12}$  and  $R_{eq}=25.0^{+0.8}_{-0.6}$ .

## 6. CONCLUSIONS

We have performed a pencil-beam search of a single Subaru ecliptic field. The search covered  $0.255 \text{ deg}^2$ , with a limiting magnitude  $R = 26.76$ . We found 20 new TNOs with magnitudes between  $R = 24.0$  and  $26.8$ . As argued by Bernstein et al. (2004), it is not surprising that our faintest detection is near our 50% efficiency threshold, given that the luminosity function is much shallower at  $R \sim 27$ .

Including other surveys in the analysis (see § 5) we derive the most likely DPL model for the luminosity function. With only 20 new objects there is an important improvement in the model's PDF from Fuentes & Holman (2008, Figure 13) to the current result (See Figure 4); due to the new detections constraining the model between  $R = 26$  and  $27$ .

The bright end power-law exponent  $\alpha_1=0.73^{+0.08}_{-0.09}$  is very close to the results of previous shallower sur-

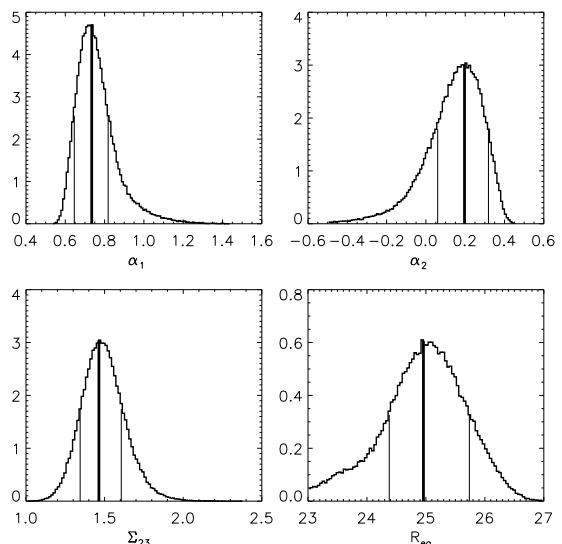


FIG. 4.— The PDF for each model's parameter. The most likely value for each parameter and 68% confidence limits are:  $\alpha_1=0.73^{+0.08}_{-0.09}$ ,  $\alpha_2=0.20^{+0.12}_{-0.14}$ ,  $\sigma_{23}=1.46^{+0.14}_{-0.12}$  and  $R_{eq}=25.0^{+0.8}_{-0.6}$ . These are plotted as vertical lines.

veys (Gladman et al. 2001). The break magnitude  $R_{eq}=25.0^{+0.8}_{-0.6}$  is more than  $1\text{-}\sigma$  fainter than the initial estimate by Bernstein et al. (2004). This is also consistent with earlier surveys reporting excellent fits to a single power model for magnitudes brighter than  $R \sim 26$  (Gladman et al. 2001). Further data between the current ground-based detection limit of  $R \sim 27$  and the HST's at  $R \sim 28.5$  will determine the break magnitude even more accurately.

Assuming that all objects are located at an heliocentric distance of 42 AU, the break in the luminosity function  $R_{eq}$  reflects a break in the size distribution  $D$ . The corresponding diameter at which the size distribution breaks

is  $D = 90 \pm 30(p/0.04)^{-0.5}$  km, where  $p$  is the albedo. Theories predict the existence of a break (Kenyon et al. 2008), but at smaller diameters ( $D \sim 20 - 40$  km). The difference reflects the uncertainty in the initial conditions for numerical simulations and the observational assumptions regarding physical properties like the albedo.

In this survey both classical and excited TNO populations are entangled. With better orbital information the size distribution of each can be studied separately. A comparison with other populations in the solar system can shed light on their origin.

## REFERENCES

- Alard, C. 2000, *A&AS*, 144, 363  
 Allen, R. L., Bernstein, G. M., & Malhotra, R. 2001, *ApJ*, 549, L241  
 Bernstein, G. & Khushalani, B. 2000, *AJ*, 120, 3323  
 Bernstein, G. M., Trilling, D. E., Allen, R. L., Brown, M. E., Holman, M., & Malhotra, R. 2004, *AJ*, 128, 1364  
 Bertin, E. & Arnouts, S. 1996, *A&AS*, 117, 393  
 Bickerton, S. J., Kavelaars, J. J., & Welch, D. L. 2008, *AJ*, 135, 1039  
 Cutri, R. M., Skrutskie, M. F., van Dyk, S., Beichman, C. A., Carpenter, J. M., Chester, T., Cambresy, L., Evans, T., Fowler, J., Gizis, J., Howard, E., Huchra, J., Jarrett, T., Kopan, E. L., Kirkpatrick, J. D., Light, R. M., Marsh, K. A., McCallon, H., Schneider, S., Stiening, R., Sykes, M., Weinberg, M., Wheaton, W. A., Wheelock, S., & Zacarias, N. 2003, 2MASS All Sky Catalog of point sources. (The IRSA 2MASS All-Sky Point Source Catalog, NASA/IPAC Infrared Science Archive. <http://irsa.ipac.caltech.edu/applications/Gator/>)  
 Davis, D. R., Farinella, P., & Weidenschilling, S. J. 1999, in *Lunar and Planetary Inst. Technical Report, Vol. 30, Lunar and Planetary Institute Conference Abstracts*, 1883  
 Elliot, J. L., Kern, S. D., Clancy, K. B., Gulbis, A. A. S., Millis, R. L., Buie, M. W., Wasserman, L. H., Chiang, E. I., Jordan, A. B., Trilling, D. E., & Meech, K. J. 2005, *AJ*, 129, 1117  
 Fraser, W. C., Kavelaars, J., Holman, M. J., Pritchett, C. J., Gladman, B. J., Grav, T., Jones, R. L., MacWilliams, J., & Petit, J. . 2008, *ArXiv e-prints*, 802  
 Fuentes, C. I. & Holman, M. J. 2008, *AJ*, 136, 83  
 Gladman, B., Kavelaars, J. J., Petit, J.-M., Morbidelli, A., Holman, M. J., & Loredano, T. 2001, *AJ*, 122, 1051  
 Holman, M. J., Kavelaars, J. J., Grav, T., Gladman, B. J., Fraser, W. C., Milisavljevic, D., Nicholson, P. D., Burns, J. A., Carruba, V., Petit, J.-M., Rousselot, P., Mousis, O., Marsden, B. G., & Jacobson, R. A. 2004, *Nature*, 430, 865  
 Ichikawa, S.-I. 2002, *Astronomical Herald*, 95, 266  
 Jones, R. L., Gladman, B., Petit, J.-M., Rousselot, P., Mousis, O., Kavelaars, J. J., Campo Bagatin, A., Bernabeu, G., Benavidez, P., Parker, J. W., Nicholson, P., Holman, M., Grav, T., Doressoundiram, A., Veillet, C., Scholl, H., & Mars, G. 2006, *Icarus*, 185, 508  
 Kavelaars, J. J., Holman, M. J., Grav, T., Milisavljevic, D., Fraser, W., Gladman, B. J., Petit, J.-M., Rousselot, P., Mousis, O., & Nicholson, P. D. 2004, *Icarus*, 169, 474  
 Kenyon, S. J. & Bromley, B. C. 2004, *AJ*, 128, 1916  
 Kenyon, S. J., Bromley, B. C., O'Brien, D. P., & Davis, D. R. 2008, *Formation and Collisional Evolution of Kuiper Belt Objects (The Solar System Beyond Neptune)*, 293–313  
 Kenyon, S. J. & Luu, J. X. 1999, *AJ*, 118, 1101  
 Miyazaki, S., Komiya, Y., Sekiguchi, M., Okamura, S., Doi, M., Furusawa, H., Hamabe, M., Imi, K., Kimura, M., Nakata, F., Okada, N., Ouchi, M., Shimasaku, K., Yagi, M., & Yasuda, N. 2002, *PASJ*, 54, 833  
 Monet, D. G., Levine, S. E., Canzian, B., Ables, H. D., Bird, A. R., Dahn, C. C., Guetter, H. H., Harris, H. C., Henden, A. A., Leggett, S. K., Levison, H. F., Luginbuhl, C. B., Martini, J., Monet, A. K. B., Munn, J. A., Pier, J. R., Rhodes, A. R., Rieke, B., Sell, S., Stone, R. C., Vrba, F. J., Walker, R. L., Westerhout, G., Brucato, R. J., Reid, I. N., Schoening, W., Hartley, M., Read, M. A., & Tritton, S. B. 2003, *AJ*, 125, 984  
 Pan, M. & Sari, R. 2005, *Icarus*, 173, 342  
 Petit, J.-M., Holman, M., Scholl, H., Kavelaars, J., & Gladman, B. 2004, *MNRAS*, 347, 471  
 Stansberry, J., Grundy, W., Brown, M., Cruikshank, D., Spencer, J., Trilling, D., & Margot, J.-L. 2008, *Physical Properties of Kuiper Belt and Centaur Objects: Constraints from the Spitzer Space Telescope (The Solar System Beyond Neptune)*, 161–179  
 Trujillo, C. A., Jewitt, D. C., & Luu, J. X. 2001, *AJ*, 122, 457  
 Yoshida, F. & Nakamura, T. 2007, *Planet. Space Sci.*, 55, 1113  
 Zhang, Z. ., Bianco, F. B., Lehner, M. J., Coehlo, N. K., Wang, J. ., Mondal, S., Alcock, C., Axelrod, T., Byun, Y. ., Chen, W. ., Cook, K. H., Dave, R., de Pater, I., Porrata, R., Kim, D. ., King, S. ., Lee, T., Lin, H. ., Lissauer, J. J., Marshall, S. L., Protopapas, P., Rice, J. A., Schwamb, M. E., Wang, S. ., & Wen, C. . 2008, *ApJ*, 685, L157